A cloud and precipitation feature database from 9 years of TRMM observations

Chuntao Liu and Edward J. Zipser

Department of Meteorology, University of Utah

Daniel J.Cecil

Earth System Science Center, University of Alabama at Huntsville

Stephen W. Nesbitt

Department of Atmospheric Sciences, University of Illinois at Urbana-Champaign

Steven Sherwood

Department of Geology and Geophysics, Yale University

Submit to Journal of Applied Meteorology and Climatology

Submitted: Aug 2007

Revised: Feb 2008

Key words: TRMM, cloud features, precipitation features

Corresponding author address: Dr. Chuntao Liu, Department of Meteorology, University of Utah

135S 1460E Rm 819, Salt Lake City, UT, 84112-0110

E-mail: liu.c.t@utah.edu

Abstract

An event-based method of analyzing the measurements from multiple satellite sensors is presented by using observations of the TRMM Precipitation Radar (PR), Microwave Imager (TMI), Visible and Infrared Sensor (VIRS) and Lightning Imaging System (LIS). First, the observations from PR, VIRS, TMI and LIS are temporally and spatially collocated. Then the cloud and precipitation features are defined by grouping contiguous pixels using various criteria, including surface rain, cold infrared or microwave brightness temperature. The characteristics of measurements from different sensors inside these features are summarized. Then, climatologies of many properties of the identified features are generated. This analysis method condenses the original information of pixel level measurements into the properties of events, which can greatly increase the efficiency of searching and sorting the observed historical events.

Using the TRMM cloud and precipitation feature database, the regional variations of rainfall contribution by features with different size and intensity and PR reflectivity vertical structure are shown. Above the freezing level, land storms tend to have larger 20 dBZ area and reach higher altitude than oceanic storms, especially those over central Africa. Horizontal size and the maximum reflectivity of oceanic storms decrease with altitude. For land storms, these intensity measures increase with altitude between 2 km and the freezing level, and decrease more slowly with altitude above the freezing level than ocean storms.

1. Introduction

As the quantity of satellite observations available for cloud and precipitation research continues to increase, more efficient methods for analysis and sorting of useful information from these observations are becoming essential. Traditionally, the orbital pixel level observations are statistically summarized onto horizontal grids and provide information on their global distribution. However, gridded averaged data products cannot be used to retrieve information on individual events. It is difficult to quickly search and fetch information of historical weather events either from these grid level datasets, or from original pixel level observations due to the huge amount of data. One solution is to summarize observations for individual cloud or precipitation events.

Event-based analysis methods are not new. There were studies of clouds by grouping pixels with the infrared brightness temperature colder than certain criteria (e.g. Mapes and Houze, 1992; Liu et al., 1995; Chen et al., 1996), studies of precipitation systems by grouping pixels with cold microwave brightness temperature (e.g. Mohr and Zipser, 1996; Toracinta and Zipser, 2001), or by grouping pixels with valid precipitation radar echoes (e.g. Geerts 1998; Lang et al. 2007; Cifelli et al., 2007). However, when several satellite instruments target the same object, different instruments and their measurands have their own characteristics and give different perspectives. Examples include Tropical Rainfall Measuring Mission (TRMM, Kummerow et al., 1998) and A-Train (Stephens et al., 2002) observations. On the TRMM satellite, the Precipitation Radar (PR) can provide detailed vertical distribution of precipitation sized particles inside systems. The TRMM Microwave Imager (TMI) can provide some information on vertically integrated ice and water path. The Visible and Infrared Scanner (VIRS) can provide information on cloud top temperature and reflectance. At the same time, the Lightning Imaging Sensor (LIS) estimates lightning flash rates. How to analyze and efficiently utilize all this information is a scientific challenge.

One way to summarize the precipitation events from the TRMM dataset is to define Precipitation Features (PFs, Nesbitt et al., 2000). This method groups the pixels with near surface PR reflectivity ≥ 20 dBZ or ice scattering signal defined by TMI 85 GHz Polarization Corrected Temperature (PCT, Spencer et al., 1989) ≤ 250 K. Using this definition and the similar feature grouping concept, results have included rainfall estimates validation (Nesbitt et al., 2004), diurnal cycle of precipitation systems (Nesbitt and Zipser, 2003), global distribution of storms with LIS-detected lightning (Cecil et al., 2005), deep convection reaching the tropical tropopause layer (Liu and Zipser, 2005), rainfall production and convective organization (Nesbitt et al. 2006), and the categorization of extreme thunderstorms by their intensity proxies (Zipser et al., 2006).

However, this particular definition of PFs has some disadvantages that limit its applicability to wider research areas. First, the PFs defined by Nesbitt et al. (2000) excludes some light rain area with surface reflectivity between the PR minimum detectable signal of 17-18 dBZ and 20 dBZ, and TMI 85 GHz PCT > 250 K. Also some PFs over non-raining areas with cold 85 GHz PCT are artifacts due to low surface emissivity from snow cover, especially over high terrain. Second, the precipitating area usually is only a small part of a cloud system. There exist large areas of cold anvil clouds neither with surface radar echoes, nor with cold ice scattering signals (Liu et al., 2007). Thus, this PF definition cannot be used to study the entire cloud system, especially the relation between the precipitation and the radiative impacts of these cloud systems. Third, it is inappropriate to compare conditional rain rates from the PR and TMI in a feature defined using information from both PR and TMI measurements (Nesbitt et al. 2004).

This paper introduces a method that reduces the above limitations by using multiple definitions of the cloud and precipitation features to analyze TRMM data. A database is constructed with features identified from 9 years of TRMM observations. Then, the regional variations of the cloud and precipitation features' rainfall contributions and their convective intensity inferred from vertical reflectivity structures are studied using the database.

2. Data and Methods

The schematic diagram of the TRMM cloud and precipitation feature database with three levels of TRMM data processing is shown in Figure 1. First, the measurements from multiple instruments are temporally and spatially collocated. Then the cloud and precipitation features are defined with different criteria using these collocated data. Using the characteristics of defined features, global climatologies of cloud and precipitation feature populations, occurrences and other statistics are generated. This section introduces the methods used in these three steps.

2.1 Level-1: Collocation of measurements from different instruments

To collocate the observations from different instruments, a common sample volume and unified coordinates has to be defined. Here we use measurements only in the Precipitation Radar swath, and choose coordinates of the PR pixels as the common grids for collocation. The collocated TRMM datasets include version 6 VIRS radiances (1B01), TMI brightness temperatures (1B11), rainfall retrievals from TMI (2A12, Kummerow et al., 2001), stratiform and convective rainfall categorizations (2A23, Steiner et al., 1995, Awaka et al., 1998), rainfall retrieval from PR (2A25, Iguchi et al., 2000) and LIS flashes (http://daac.gsfc.nasa.gov/data/datapool/TRMM/).

Since both VIRS and PR scan through nadir, the brightness temperatures at five VIRS channels at each PR pixel are calculated from radiances at the nearest neighbor VIRS pixel. Each LIS flash is also assigned to a PR pixel by using the nearest neighbor method. Because TMI scans conically and the measurements at different wavelengths have different resolutions, the collocation between TMI and PR measurements are not as simple. TRMM 1B11 orbital granule data are stored in two resolutions. One is the low resolution with pixel area ~ 96 km^2 (13. x 7.3) before the TRMM satellite orbit boost in August 2001 and ~ 110 (13 x 8.3) km^2 after the boost for 10, 19, 21, 37 GHz brightness temperatures. The other is the high resolution with pixel size ~ 48 km^2 (13 x 3.65) before the boost and ~ 55 km^2 (13 x 4.2) after the boost for 85GHz brightness temperatures and rain retrievals. Note that these are the sizes of the areas between each measurement location; the instrument field of view is smaller than the distance between scans for 85 GHz while the field of view becomes sequentially larger for each of the lower frequencies (Kummerow et al. 1998) to the point where the 10 GHz channel is much larger than the gap between low resolution scans (e.g., oversampling). The collocations are performed on both resolutions inside the PR swath. Using the nearest neighbor method, each PR pixel is assigned a corresponding TMI pixel with parameters from 1B11 and 2A12. Because of the differing spatial resolutions, multiple PR pixels are assigned to a single TMI pixel.

Because TMI scans with a conical 52.8^o incidence angle, there is usually a collocation problem if the microwave ice scattering signals are from elevated hydrometeors. For example, as shown in Figure 2, the scattering signal from ice particles at about 12.7 km would seem as from the neighbor pixel in the previous scan. To account for this, we used a rough parallax correction method that simply moves the coordinates of TMI data backwards (or forwards depending on the orientation of the scan) for one scan as shown in Figure 2. After this correction, there are better location correspondences between PR and TMI observations for deep convective cells with strong ice scattering. However, the correspondence for shallow precipitation inevitably becomes worse because of this overcorrection. This leads to problems when summarizing TMI measurements inside a small and shallow precipitation system. Limiting such problems is one reason we focus on comparing properties of larger cloud and precipitation events, as opposed to comparing individual pixels. After collocation, the selected parameters (Some are listed in Section 2.2; Liu, 2007) are saved into compressed orbital files in Hierarchical Data Format 4 (HDF4) format as level-1 products.

2.2 Level-2: Defining cloud and precipitation features

Using the collocated level-1 products, a set of cloud and precipitation features are defined using the criteria listed in Table 1. In addition to the prior PF definition (Nesbitt et al., 2000), two “pure” precipitation feature definitions are introduced by contiguous 2A25 near surface raining pixels (RPFs) and contiguous 2A12 surface raining pixels (TPFs). To fully utilize the three dimensional information from PR reflectivity profiles, Radar Projection Precipitation Features (RPPFs) are introduced by grouping the area of ground projection of radar reflectivity greater than 20 dBZ, which includes thick anvils aloft. Cold PCT features (PCTFs) are also defined by pixels with 85 GHz PCT < 250 K, for continuity with the longer record of SSM/I measurements. Cloud features are defined by using VIRS 10.8 μm brightness temperature (T_{B11}) < 210 K (C210F), 235 K (C235F) and 273 K (C273F). Characteristics of features are summarized from measurements and retrievals from PR, TMI, VIRS and LIS at the grouped pixels. In addition to the time and centroid location, some of the major parameters stored are listed below (Details in Liu, 2007):

- From PR algorithm 2A25 and 2A23, we calculate stratiform and convective rain area and volume (Units in mm/hour·km^2) from 2A25 near surface rain rate retrieval; maximum height of 20, 30, and 40 dBZ; vertical profile of maximum reflectivity with 0.5 km resolution; vertical profile of 20 dBZ area with 1 km resolution. The vertical profiles are calculated after interpolating the 2A25 attenuation corrected reflectivity factor from slant path bins to each vertical level relative to the Earth surface.
- From TMI algorithm 1B11 and 2A12, we calculate rain area and volume; Minimum 37 GHz and 85 GHz PCTs; area of 85 GHz PCT < 250 K, 200K, 150 K and 100 K.
- From VIRS algorithm 1B01, we calculate minimum T_{B11}; area of T_{B11} < 210, 235, and 273 K; and median value of brightness temperature at 5 wavelengths.
- From LIS, we accumulate the lightning flash count and view time (duration of observation, normally around 80 s) for the feature. Together, these yield a flash rate.

- To examine the environment of a cloud or precipitation feature, vertical profiles of temperature, geopotential height, wind and humidity are extracted from the 6 hourly 2.5^{o} x 2.5^{o} NCEP reanalysis dataset (Kalnay et al. 1996; Kistler et al., 2001) for each feature with at least 4 PR pixels. First we temporally interpolate the NCEP data to the feature time. Then the data at the nearest neighbor of NCEP grid to the feature center are selected. Due to the coarse temporal and spatial resolution of NCEP reanalysis, and also because we do not take care to select a grid point representative of "inflow air" for each feature, these data should be used with caution.

An example of feature definitions for a severe storm over Oklahoma (Zipser et al., 2006) and some parameters in the defined RPPF are shown in Figure 3. In this case, there were large areas of thick anvil aloft (Figure 3b, 3e) and large areas of cold clouds, without a strong ice scattering signal (Figure 3d) and hardly any surface rain (Figure 3a). The old precipitation feature definition would mostly neglect the information about the anvil cloud. However, the detailed vertical distribution of 20 dBZ area can be summarized in RPPFs (Figure 3f). As shown in Table 2, the system can be described more comprehensively with multiple feature definitions. For example, the ratio from the large cold cloud area to surface raining area can be described by cold cloud features (C210, C235F and C273F); the differences between 2A25 and 2A12 rain volume may be used to validate the performance of rain retrieval algorithms; etc.

The original orbital level-1 data has a typical file size of about 200 megabytes. However, the information of the observed events in the orbit can be condensed into properties of features with file size of, on average, 2.8 megabytes, a reduction in data volume by a factor of 72. After all features are defined from level-1 orbital products, they are combined into monthly files in HDF4 format as level-2 products.

2.3 Level-3: Generating climatology from cloud and precipitation features

It is useful to have characteristics of individual clouds and precipitation systems in Level-2 data. It is also important to study the climatologies of characteristics of these systems. For this purpose, we summarize the statistics of feature properties onto a 1^{o}x1^{o} grid, such as the total volumetric rain, the maximum reflectivity found over a specific region, etc. Because TRMM observations include information of the diurnal variation of properties of cloud and precipitation systems, they are categorized into 8 local time periods.

Note that when we accumulate the rain volume from features onto the grids, volumetric rain and area inside each feature are assigned to the grid where the mass-weighted centroid of that feature is located. This could be problematic when we assign volumetric rain and raining area from large cloud and precipitation features to a small grid. However, given enough samples, this problem is minimized to some extent. As shown in Figure 4, the general pattern of monthly rainfall by counting the raining pixels inside the grids (3A25) and that by accumulating rain volume of precipitation features centered inside the grids are very close. The differences between the two become smaller when using larger grids (Figure 4d). However, this problem is noticeable when large systems systemically center at certain locations over some regions, such as Panama and Argentina (Figure 4d).

To compare with the precipitation estimates from other sources, besides the parameters summarized from features, we also combined TRMM 3B43, 3A25 (gridded monthly rainfall from 2A25), and 3A12 (gridded monthly rainfall from 2A12) precipitation products, and the rainfall estimates from GPI (Joyce, 1997), GPCC (Rudolf, 1995), GPCP (Huffman et al, 2001) onto the same grid. Then level-3 data are produced with all different rainfall estimates and statistically summarized properties of features. Some major parameters calculated in level-3 monthly products are listed below (details in Liu, 2007):

- Monthly rainfall estimates from GPI, GPCC, GPCP, TRMM 3B43, 3A25, and 2A25 and 2A12 rain volume inside the features; total 2A25 convective and stratiform raining area and rain volume; rain volume inside features during 8 local times;total number of PR observations.
- Population of features. Total flash counts, total area of T_{B11} < 210 K, 235 K and 273 K, total area of 85 GHz PCT < 250 K, 200 K, 150 K, and 100 K during 8 local times inside features. Total 20 dBZ area at different altitudes.
- Maximum 20 dBZ, 30 dBZ, 40 dBZ echo tops, maximum flash counts, maximum reflectivity at different altitudes, minimum T_{B11} and 37 GHz, 85 GHz PCT inside a feature during 8 local time periods (0-3, 3-6, 6-9, …).

Level-3 products are processed for monthly, yearly, before boost (January 1998- July 2001), after boost (September 2001-December 2006), seasonally (DJF, MAM, JJA, SON), and 9 year (1998-2006).

2.4 Impact of the satellite orbit boost

After the TRMM satellite orbit height was boosted from 350 km to 403 km August 2001, not only had averaged effective pixel areas in 1B01, 1B11 and 2A25 increased about 15%, but the orbit boost also led to changes in many observed and retrieved properties, such as amount of precipitation (e.g., DeMoss and Bowman, 2007). One immediate impact of a larger footprint is a more serious beam filling problem. One would expect that the TMI and the PR would have lower sensitivity after the boost because a larger footprint has higher possibility to include background radiance over non-precipitating area, while the sensitivity of the PR decreased as well because of an increased range to target. The height of the lowest PR valid bin above the terrain also increased due to the larger footprint. Larger instrument fields of view may also introduce pre and post boost inconsistency in the parallax correction and collocation between PR and TMI. With more than 10 years of TRMM observations, it is possible to study the long term change of the properties of the features. How to separate the natural climate variability from the influences of orbit boost in TRMM measurements is a major challenge. Therefore, research regarding the impact of the boost on the sensitivity of the TRMM instruments is warranted in the future.

3. Applications

In this section, we introduce three applications of the 9-year (1998-2006) TRMM cloud and precipitation feature database.

3.1 Search engine for the specific cases

The example (Figure 3) demonstrated that TRMM level-1 and level-2 products are powerful tools for case studies by providing the collocated observations and the characteristics of the target features. But how do we find the interesting cases? Besides providing the characteristics of a given event, one immediate use of the level-2 dataset is to search for historical events with certain properties for a given region. For example, how many events were there with at least 2000 km^2 PR raining area and 50 flashes observed by LIS during the past 9 years near Panama? It is easy to answer this question (total 5 MCSs from 1998 to 2006 in 80^o-85^{o}W and 8^o-10^{o}N) by searching through the level-2 datasets rather than by the almost impossibly lengthy process of looking through all the orbital pixel level data. An example of such a searching tool is publicly available online at http://www.met.utah.edu/trmm/ for TRMM observed MCSs during 1998-2006. Using level-2 products, we may also sort and categorize the defined features, such as the most intense convective storms (Zipser et al., 2006), the rainiest storms, or the coldest clouds, etc..

3.2 Populations and sizes of cloud and precipitation features and their contribution to rainfall

One important application of TRMM cloud and precipitation feature database is to study the rainfall contributed from specific types of precipitation systems. By dividing the total population and rain volume from the selected subset of features to those from all features, the importance of the subset of features to the total rainfall can easily be evaluated. For example, consistent with Nesbitt et al., 2006, precipitation systems having size of 2000 km^2 or more constitute less than 2% of total population of detectable (at least one pixel with ~20 km^2 in size) precipitation systems (Figure 5a), but contribute more than 60% of total rainfall over the most rainy areas of the tropical oceans (Figure 5b). Over oceans, flashes are rarely seen. However, the subtropical oceanic precipitation systems having flashes contribute around 10% of total rainfall there (Figure 5c and 5d). Over tropical land, precipitation systems with flashes contribute a larger part of the total rainfall over Central Africa than over Amazon and Indonesia. Shallow and warm raining systems are the main contributors to the rainfall over the less rainy oceanic regions (Figure 5e and 5f) (Schumacher and Houze 2004). Very cold cloud tops (T_{B11}< 210 K) are almost twice as likely over Central Africa, Panama, Northern Australia and southern Mexico than over the Amazon, and rainfall under these cold clouds is about 50% of the total over these regions. Over oceans, the West Pacific is more likely to have very cold clouds (Figure 5g and 5h). The original technique of estimating the rainfall from satellite infrared images is to relate the rainfall to the area of T_{B11} brightness temperature colder than 235 K (Arkin and Meisner, 1987). However, on average, less than one third of precipitation systems over land and less than one fifth of oceanic systems have minimum cloud top temperature colder than 235 K. On average, less than 50% of the rainfall comes from clouds colder than 235 K (Figure 5i and 5j). There are more precipitation systems with ice scattering signatures (85 GHz PCT < 250 K, Spencer et al., 1989) over land than over ocean (Figure 5k). However, the percentage of rainfall from under the cold PCT area over the Amazon is close to that over most of the ocean (Figure 5l). Notice that in Figure 5i and 5k, there is a large number of RPFs with minimum T_{B11} < 235 K and minimum 85 GHz PCT < 250 K over Tibet. Those RPFs are mostly artifacts due to low emissivity at infrared and microwave wavelengths over cold (snow) surfaces.

To quantitatively demonstrate the regional variations of the precipitation feature sizes, intensities and their contribution to the total rainfall, the Cumulative Distribution Functions (CDFs) of population and rainfall contribution as a function of system size and intensity (defined using minimum PCT) of RPFs are calculated for the selected five regions over land and four regions over ocean (Figure 6a). Over ocean, the percentage of small size RPFs (and their corresponding rainfall contributions) is greater than over land. RPFs smaller than 1000 km^2 constitute ~90% of the population but contribute less than 20% of the rainfall. RPFs greater than 10000 km^2 contribute more than 60% of total rainfall over SPCZ, around 50% over tropical ocean (Figure 6b). Based on the convective intensity inferred from ice scattering signature of 85 GHz PCT, oceanic RPFs are convectively weaker than those over land with warmer 85 GHz PCTs. Compared to other regions, warm RPFs with 85 GHz PCT > 200 K over the SPCZ contribute the largest percentage of rainfall (Figure 6c).

Over land, RPFs greater than 10000 km^2 contribute 70% of total rainfall over Argentina and South East US, and about 40% over the Amazon. The Congo Basin has the greatest percentage of RPFs with intense 85 GHz ice scattering. However, CDFs of rainfall contribution over the Congo, Argentina and South East US are very different from those of Amazon and Indonesia; the latter two are closer to CDFs from tropical oceans. RPFs with minimum 85 GHz PCT < 100 K (150 K) contribute around 15% (50%) of total rainfall over Congo, Argentina and South East US, but less than 5% (30%) over Amazon, Indonesia and oceans.

By varying the feature definition, a different perspective of precipitation contribution from under cold clouds (e.g., Liu et al., 2007) or systems with cold 85 GHz PCT can be studied. For example, the total rainfall contributions and the contributions from the largest 1% of features differently defined are listed in Table 3. The differences between the rainfall contribution from TPFs and RPFs are caused by the different rainfall screening algorithms and by uncertainties in the collocation of TMI and PR pixels. The rainfall under the cloud colder than 235 K only contributes 57% to the total rainfall over the tropics (20°S – 20°N).

3.3 Regional variations of vertical structure of radar echoes

Another application of the TRMM feature database is to study the regional variations of vertical structures of precipitation features. Figure 7 shows the 20 dBZ echo occurrence calculated by dividing the 20 dBZ area inside RPPFs at selected heights by the total PR sampled area during 1998-2006. At 2 km height, 20 dBZ echoes occur more frequently over ocean than over land. At 5 km, 20 dBZ echoes occur more over west Pacific and Indonesia than other places. At 9 km, there are more 20 dBZ echoes over land than over ocean. At 13 km, 20 dBZ echoes over land dominate (Liu and Zipser 2005).

Focusing on the strong RPPFs with 40 dBZ echo and 1000 km^2 in size, the Contoured Frequency by Altitude Diagrams (CFADs, Yuter and Houze 1995) of 20 dBZ area profiles of these RPPFs from 20^oS-20^oN are shown in Figure 8. In general, oceanic systems have larger 20 dBZ area below 2 km than land systems. However, due to the ground clutter, the 20 dBZ area below 2 km over land and below 1.5 km over ocean may be compromised. Oceanic RPPFs 20 dBZ areas decrease faster with altitude than those of land RPPFs above 2 km. Half of the strong oceanic RPPFs have 100 km^2 20 dBZ area above 8 km, and half of the strong land RPPFs have 100 km^2 20 dBZ area above 9.5 km. It is interesting that between 2 km and 4 km, 20 dBZ area increases with altitude in RPPFs over land, while 20 dBZ area decreases with altitude in RPPFs over ocean.

CFADs of maximum reflectivity profiles of the RPPFs with 40 dBZ echo and 1000 km^2 in size are shown in Figure 9. Land RPPFs have larger maximum reflectivity values than oceanic RPPFs at the freezing level (4-5 km). Then the land RPPF maximum reflectivity values decrease more slowly than oceanic RPPFs above the freezing level, while reaching higher altitudes. Half of the land (ocean) RPPFs have maximum reflectivity values > 20 dBZ at 11.5 km (10 km). From 2 km to the freezing level near 5 km, the maximum reflectivity of land RPPFs increases with altitude, but that of the oceanic RPPFs decreases with altitude. This is consistent with the result of the maximum reflectivity profiles of MCSs described by Zipser and Lutz (1994) using ground-based radar data from a few locations.

To demonstrate regional variations, CFADs of 20 dBZ area and maximum reflectivity profiles are analyzed for RPPFs containing at least one pixel > 40 dBZ echo and is 1000 km^2 in size in the selected regions shown in Figure 6a. The median profiles of those CFADs are compared in Figure 10. Above the freezing level, land RPPFs have larger 20 dBZ area and reach higher altitudes than oceanic RPPFs. On average, RPPFs over the Congo Basin are the tallest, strongest (Zipser et al., 2006) and the largest in the tropics. Extra-tropical systems in SE US and Argentina are even larger. From 2 km to the freezing level, maximum reflectivity and 20 dBZ area of oceanic RPPFs decrease with altitude, in contrast to the RPPFs in all land regions. Southeast US and Argentina RPPFs have larger 20 dBZ area and stronger reflectivity near 2 km. Congo has the largest increase of maximum reflectivity and 20 dBZ area below from 2 km to freezing level. This may be explained by strong evaporation below clouds over the region (McCollum et al., 2000; Geerts and Dejene 2005). Acting similar to a "green ocean" (Silva Dias et al., 2002), the

Amazon has the smallest increase of maximum reflectivity and a slight decrease of 20 dBZ area from 2 km to freezing level.

One additional factor that has to be considered when interpreting Figures 9 and 10 is the PR's attenuation (and its correction), which increases towards the surface at greater range from the radar. Reflectivity may be attenuated severely under the strongest convective cores, so any errors in the attenuation correction algorithm for the PR would lead to increased uncertainty in determining maximum reflectivities at lower altitudes. Following this reasoning, however, projected area of 20 dBZ should be influenced to a much lesser extent,

Summary

This paper introduces the construction and applications of a database containing cloud and precipitation features identified from measurements of radar, and visible, infrared and microwave radiometers onboard the TRMM satellite. First, the measurements from different instruments are collocated and level-1 products are generated with common coordinates for the different measurements. Then by defining the cloud and precipitation features in level-2 products, original information of pixel level measurements is compressed into the characteristics of features, which may easily be used to index the observed events. This increases substantially the efficiency of searching and sorting the observed historical events. The level-3 products are generated by summarizing the characteristics of features onto 1^{o}x1^{o} grids and provide useful climatologies of rainfall and properties of the contributing cloud and precipitation systems.

Besides indexing the cloud and precipitation features, two applications of examining rainfall contribution and regional differences of vertical structure of convection are explored by using the feature database. There are many other possible studies, such as validation of rainfall retrieval algorithms from PR and TMI measurements, differences among the diurnal cycles of lightning, cloud coverage and precipitation, and validation of properties of convection and convective systems in climate models. Those topics will be discussed in future studies.

In all, we introduced a method of analyzing the measurements from multiple instruments on board TRMM by defining multiple types of features to summarize the information of the observed event. The general framework of this method can be applied to other multiple instrument measurements, such as observations from the A-Train, which consist of data from several satellites flying on the same orbital path, often measuring the same objects.

Acknowledgement

This research was supported by NASA Precipitation Measurement Mission grants NAG5-13628 and NN-H-06-Z-DA-001-N to CL and EZ under the direction of Dr. Ramesh Kakar. Special thanks go to Drs. Erich Stocker and John Kwiatkowski and the rest of the TRMM Science Data and Information System (TDSIS) at NASA Goddard Space Flight Center, Greenbelt, MD, for data processing assistance.

References

Arkin, P. A., and B. N. Meisner. 1987: The relationship between large-scale convective rainfall and cold cloud over the western hemisphere during 1982-84. *Mon. Wea. Rev.* **115**, 51–74.

Awaka, J., T. Iguchi, and K. Okamoto, 1998: "Early results on rain type classification by the Tropical Rainfall Measuring Mission (TRMM) precipitation radar", Proc. 8th URSI Commission F Open Symp., Aveiro, Portugal, pp.143-146**.**

DeMoss, J. D. , and K. P. Bowman, 2007: Changes in TRMM rainfall due to the orbit boost estimated from buoy rain gauge data, *J. Atmos. Oceanic Tech*., **24**, 1598-1607.

Cecil, D. J., S. J. Goodman, D. J. Boccippio, E. J. Zipser and S. W. Nesbitt, 2005: Three years of TRMM precipitation features. Part I: radar, radiometric, and lightning characteristics, *Mon. Wea. Rev.* **133**, 543–566.

Chen, S., R. A. Houze Jr., and B. E. Mapes, 1996: Multiscale variability of deep convection in relation to large-scale circulation in TOGA COARE, *J. Atmos. Sci.*, **53**, 1380-1409.

Cifelli, R., S. R. Nesbitt, S. A. Rutledge, W. A. Petersen, and S. Yuter, 2007: Radar characteristics of precipitation features in the EPIC and TEPPS regions of the east Pacific, *Mon. Wea. Rev.*, **135**, 1576-1595.

Geerts, B., 1998: Mesoscale Convective Systems in the Southeast United States during 1994–95: A Survey. *Wea. Forecasting*, **13**, 860-869.

Geerts,B., and T. Dejene, 2005: Regional and diurnal variability of the vertical structure of precipitation systems in Africa based on spaceborne radar data. *J. Climat.*, **18**, 893-916.

Huffman, G., R. Adler, M. Morrissey, D. Bolvin, S. Cuttis, R. Joyce, B. McGavock and J.Susskind, 2001: Global precipitation at one degree resolution from multi satellite observations. *J. Hydrometeor.,* **2**, 36-50.

Iguchi, T., T. Kozu., R. Meneghini, J. Awaka, and K. Okamoto, 2000: Rain-profiling algorithm for the TRMM precipitation radar. *J. Appl. Meteor.*, **39**, 2038-2052.

Joyce, R., and P. A. Arkin, 1997: Improved estimates of tropical and subtropical precipitation using the GOES Precipitation Index. *J. Atmos. Ocean. Tech.*, **10**, 997-1011.

Kalnay, E., M. Kanamitsu, R. Kistler, W. Collins, D. Deaven, L. Gandin, M. Iredell, S. Saha, G. White, J. Woollen, Y. Zhu, A. Leetmaa, B. Reynolds, M. Chelliah, W. Ebisuzaki, W. Higgins, J. Janowiak, K. C. Mo, C. Ropelewski, J. Wang, R. Jenne, and D. Joseph, 1996: The NCEP/NCAR 40 year reanalysis project, *Bull. Amer. Meteor. Soc.*, **77**, 437-471.

Kistler, R., E. Kalnay, W. Collins, S. Saha, G. White, J. Woollen, M. Chelliah, W. bisuzaki, M. Kanamitsu, V. Kousky, H. Dool, R. Jenne and M. Fiorino, 2001: The NCEP-NCAR 5—year reanalysis: monthly means CD-ROM and documentation. *Bull. Amer. Meteor. Soc.* **82**, 247-267.

Kummerow, C., W. Barnes, T. Kozu, J. Shiue, and Joanne Simpson, 1998: The Tropical Rainfall Measuring Mission (TRMM) Sensor Package. *J. Atmos. Oceanic Tech.,* **15**, 809–817.

Kummerow, C., Y. Hong, W. S. Olson, S. Yang, R. F. Adler, J. McCollum, R. Ferraro, G. Petty, D.-B. Shin, and T. T. Wilheit. 2001: The Evolution of the Goddard Profiling Algorithm (GPROF) for rainfall estimation from passive microwave sensors. *J. Appl. Meteor.,* **40**, 1801–1820.

Liu, C., and E. J. Zipser, 2005: Global distribution of convection penetrating the tropical tropopause, *J. Geophys. Res.*, doi:10.1029/2005JD00006063.

Liu, C., E. Zipser, and S. W. Nesbitt, 2007: Global distribution of tropical deep convection: Different perspectives using infrared and radar as the primary data source, *J. Climate*, **20**, 489-503.

Liu, C., University of Utah TRMM precipitation and cloud feature database description, v1.0, http://www.met.utah.edu/trmm/TRMM_database_description_v1.0.pdf, 2007.

Liu, G., J. A. Curry, R. Sheu, 1995: Classification of clouds over the western equatorial Pacific Ocean using combined infrared and microwave satellite data, *J. Geophys., Res.*, **100**, 13811-13826.

Mapes, B. E., and R. A. Houze, 1992: Cloud clusters and superclusters over the oceanic warm pool. *Mon. Wea. Rev.*, **121**, 1398-1416.

McCollum, J., A. Gruber, and M. B. Ba, 2000: Discrepancy between Gauges and Satellite Estimates of Rainfall in Equatorial Africa. *J. Appl. Meteor.,* **39**, 666–679.

Mohr, K. I., and E. J. Zipser, 1996: Mesoscale convective systems defined by their 85-GHz ice scattering signature: Size and intensity comparison over tropical oceans and continents, *Mon. Wea. Rev.*, **124**, 2417-2437.

Nesbitt, S. W., E. J. Zipser, and D. J. Cecil, 2000: A census of precipitation features in the tropics using TRMM: radar, ice scattering, and lightning observations. *J. Climate*., **13**, 4087-4106.

--------, and E. J. Zipser, 2003: The diurnal cycle of rainfall and convective intensity according to three years of TRMM measurements. *J. Climate.*, **16**, 1456–1475.

--------, S. W., R. Cifelli, and S. A. Rutledge, 2006: Storm morphology and rainfall characteristics of TRMM precipitation features, *Mon. Wea. Rev*., **134**, 2702-2721.

Rudolf, B., 1995: Global Precipitation Climatology Centre. In: WMO/UNEP, The global climate system review, climate system monitoring June 1991 - November 1993. *WMO-No. 819, Genf*, 37.

Silva Dias, M. A. F., S., and coauthors, 2002: Cloud and rain processes in a biosphere-atmosphere interaction context in the Amazon region, *J. Geophys., Res*., **107**, doi:10.1029/2001JD000335.

Spencer, R. W., H. G. Goodman, and R. E. Hood, 1989: Precipitation retrieval over land and ocean with the SSM/I: identification and characteristics of the scattering signal. *J. Atmos. Oceanic Tech.*, **6**, 254-273.

Steiner, M., R. A. Houze Jr., and S. Yuter, Climatological characterization of three-dimension storm structure from operational radar and rain gauge data, *J. Appl. Meteor.*, **34**, 1978-2007.

Stephens, G. L., and coauthors, 2002: The CloudSat mission and the A-TRAIN, *Bull. Amer. Meteor. Soc.*, **83**, 1771-1790.

Toracinta, E. R., and E. J. Zipser, 2001: Lightning and SSM/I-ice-scattering mesoscale convective systems in the global tropics, *J. Appl. Meteor.*, **40**, 983-1002.

Yuter, S. E., and R. A. Houze, 1995: Three-dimensional kinemetic and microphysical evolution of Florida cumulonimbus. Part II: Frequency distributions of vertical velocity, reflectivity, and differential reflectivity, *Mon. Wea. Rev.*, **123**, 1941-1963.

Zipser, E. J., and K. R. Lutz, 1994: The vertical profile of radar reflectivity of convective cells: A strong indicator of storm intensity and lightning probability? *Mon. Wea. Rev.*, **122**, 1751-1759.

--------, D. Cecil, C. Liu, S. Nesbitt, and D. Yorty, 2006: Where are the most intense thunder storms on earth?, *Bull. Amer. Meteor. Soc.* , **87**, 1057-1071.

Figure captions:

Figure 1. Flow chart of three levels of the University of Utah TRMM feature database. Here TMI T_b at V10, H10, V19, H19, V21, V37, H37, V85 and H85 stands for the vertical and horizontal polarized 10, 19, 21, 37 and 85 GHz brightness temperatures. VIRS Tb at Ch1-5 stands for the VIRS observed brightness temperatures at 0.65, 1.61, 3.75, 10.8, 12.0 µm wavelengths. This dataset is open to the public; anyone interested is encouraged to contact the authors for details.

Figure 2. Schematic diagram of parallax correction. When there are hydrometeors at high altitude, the TMI microwave scattering signal would appear as from the nearby surface due to the 52^o slant angle. To account this effect and better collocate to the nadir observations, the TMI data coordinates are simply moved backwards (or forward depending on the orientation of the satellite) for one scan.

Figure 3. Demonstration of the feature types using a severe hail storm case (Zipser et al., 2006). a) 2A25 near surface rainfall rate. RPF is defined by the area with rain shown by black contour. b) PR maximum reflectivity ground projection. RPPF is defined by area with 20 dBZ shown by black contour. c) 2A12 surface rainfall rate. TPF is defined by area with rain shown by black contour. Black dots are the location of flashes detected by LIS. d) TMI 85 GHz PCT. PCTF is shown by 250 K contour line. e) VIRS T_{B11}. C210F, C235F and C273F are defined by area with $T_{B11} < 210$ K, 235 K and 273 K shown by black contours. f) Vertical profiles of 20 dBZ area and the maximum reflectivity of the large RPPF defined in b). The dash line in each panel is the edge of the PR swath. Note that there could be truncation effect due to narrow PR swath in defining large features (Nesbitt et al., 2006).

Figure 4. a) Mean TRMM 3A25 monthly rainfall from 1998-2006. b) Mean monthly rainfall from RPFs from 1998-2006. c) differences between (a) and (b). d) The differences between (a) and (b) after degrading them to $4^{o}x4^{o}$ resolution. Here negativevalues in c) and d) imply that more large precipitation systems are centered in the box so that the rainfall from nearby boxes has been counted in. Positive values in c) and d) imply that part of the rainfall in the box is from the large precipitation systems centered at nearby locations.

Figure 5. Distribution of population percentage of selected features to detectable features (at least with one PR pixel in size) and their regional rainfall contributions from 1998-2006 TRMM data. a) Population percentage of RPFs with size above 2000 km^2. b) Rainfall contribution from 2000 km^2 RPFs. c) Population percentage of RPFs with flashes. d) Rainfall contribution from RPFs with flashes. e) Population percentage of RPFs with minimum VIRS $T_{B11} > 273$ K. f) Rainfall contribution from RPFs minimum VIRS $T_{B11} >$ 273 K. g) Population percentage of RPFs with minimum VIRS $T_{B11} < 210$ K. h) Rainfall contribution from area with VIRS $T_{B11} < 210$ K (rainfall contribution from all C210Fs). i) Population percentage of RPFs with minimum VIRS $T_{B11} < 235$ K. j) Rainfall contribution from area with VIRS $T_{B11} < 235$ K (rainfall contribution from all C235Fs). k) Population percentage of RPFs with minimum TMI 85 GHz PCT < 250 K. l) Rainfall contribution from area with TMI 85 GHz PCT < 250 K (rainfall contribution from all PCTFs). Note that the scales change for the left panels (a,c,e,g,i,k).

Figure 6. a) Map showing selected regions of interest. b) Cumulative distribution functions of sizes of the RPFs with at least 4 pixels and their rainfall contribution over the selected regions. c) Cumulative distribution functions of convective intensity of RPFs with at least 4 pixels inferred from 85 GHz PCT and their rainfall contribution over the selected regions.

Figure 7. Occurrence of PR radar reflectivity above 20 dBZ at 1, 5, 9, and 13 km. The area of 20 dBZ are summarized from RPPFs in 1998-2006. Units are in %. Note that these heights are above the earth ellipsoid, so panel (a) cannot have echoes in regions of moderate terrain. Note that the scales are different for each panel.

Figure 8. a) Frequency of 20 dBZ area at different altitudes from 1998-2005 20^{o}N-20^{o}S oceanic RPPFs with at least one 40 dBZ pixel and 1000 km^2 raining area. Median (solid line), top 10% (dot line) and bottom 10% (dash line) of 20 dBZ area values at different altitudes are shown. The frequency is calculated by determining the histogram of area of all RPPFs (including those with 0 km^2 area) at each altitude levels. Right panel shows the total number of non-zero RPPF samples with 20 dBZ at different altitudes. b) same as a), but for the RPPFs over land.

Figure 9. a) Frequency of maximum reflectivity at different altitudes from 1998-2005 20^{o}N-20^{o}S oceanic RPPFs with at least one 40 dBZ pixel and 1000 km^2 raining area. Median (solid line), top 10% (dot line) and bottom 10% (dash line) of maximum reflectivity values at different altitudes are shown. The frequency is calculated by determining the histogram of area of all RPPFs (including those without echoes) at each altitude levels. Right panel shows the total number of RPPF non-zero samples at different altitudes. b) same as a), but for the RPPFs over land. Note that the number of samples decreases sharply due to ground clutter contamination below 1.5 km over ocean and below 2 km over land.

Figure 10. a) Median values of maximum reflectivity profiles from 1998-2006 RPPFs inside the selected regions shown in Figure 6a. The Median values are calculated in same way as the solid line shown in the left panel of Figure 8a) except from the RPPFs in the selected regions. b) same as a), but for the median values from 20 dBZ area profiles.

Table 1. Definition of precipitation and cloud features from 1998-2006 in University of Utah TRMM database. The populations of features are also listed.

Acronyms	Definition	Criteria	Population (millions)
RPF	Radar Precipitation Feature	Pixels with 2A25 rainfall rate >0	78.2
RPPF	Radar Projection Precipitation Feature	Pixels with 20 dBZ anywhere above ground	68.6
TPF	TMI Precipitation Feature	Pixels with 2A12 rainfall rate > 0	14.8
PCTF	TMI cold 85 GHZ PCT Feature	Pixels with 85 GHZ PCT < 250 K	6.2
C210F	Cloud Features with 210 K	VIRS T_{B11} < 210 K	2.8
C235F	Cloud features with 235 K	VIRS T_{B11} < 235 K	20.5
C273F	Cloud features with 273 K	VIRS T_{B11} < 273 K	77.2

Table 2. Some parameters of the largest features differently defined in Figure 3a-e. Note that due to 2A12 missing rain rate in the center of the system, TPF has lower values of total rain volume and missed the highest echo top of the system.

Feature definition	RPF	TPF	RPPF	PCTF	C210F	C235F	C273F
Longitude (^{o})	-97.5	-97.0	-96.8	-97.4	-97.2	-95.7	-95.3
Latitude (^{o})	34.2	34.5	34.5	34.2	34.4	35.0	35.0
Area (km^2)	4605	14694	22167	8189	14640	58885	79080
2A25 volumetric rain (mm/hr·km^2)	44963	13534	65766	45090	44710	112211	113236
2A12 volume rain (mm/hr·km^2)	98053	135469	196577	118071	127791	364781	367949
Raining area fraction (%)	100	29	39	60	38	26	20
Convective raining area fraction (%)	70	31	58	69	62	53	54
Convective rain volume fraction (%)	97	87	96	97	96	95	95
Minimum 85 GHz PCT (K)	50.3	66.8	50.3	50.3	50.3	50.3	50.3
Minimum T_{B11} (K)	190.3	193.8	187.0	190.3	190.3	187.0	187.0
Maximum storm height (K)	18.4	16.1	18.8	18.4	18.4	18.7	18.7
Flash counts (#)	400	264	514	434	427	636	636

Table 3. Contributions from all features and contributions from the largest 1% features differently defined to total rainfall over 20^{o}S- 20^{o}N.

%	Total contribution	Contribution over land	Contribution over ocean	Contribution from the largest 1%	Largest 1% over land	Largest 1% over ocean
RPF	100	100	100	66	59	67
TPF	74	68	75	42	30	46
PCTF	37	40	36	13	12	13
C210F	25	27	24	11	10	11
C235F	57	61	55	39	36	40
C273F	83	92	80	72	78	69

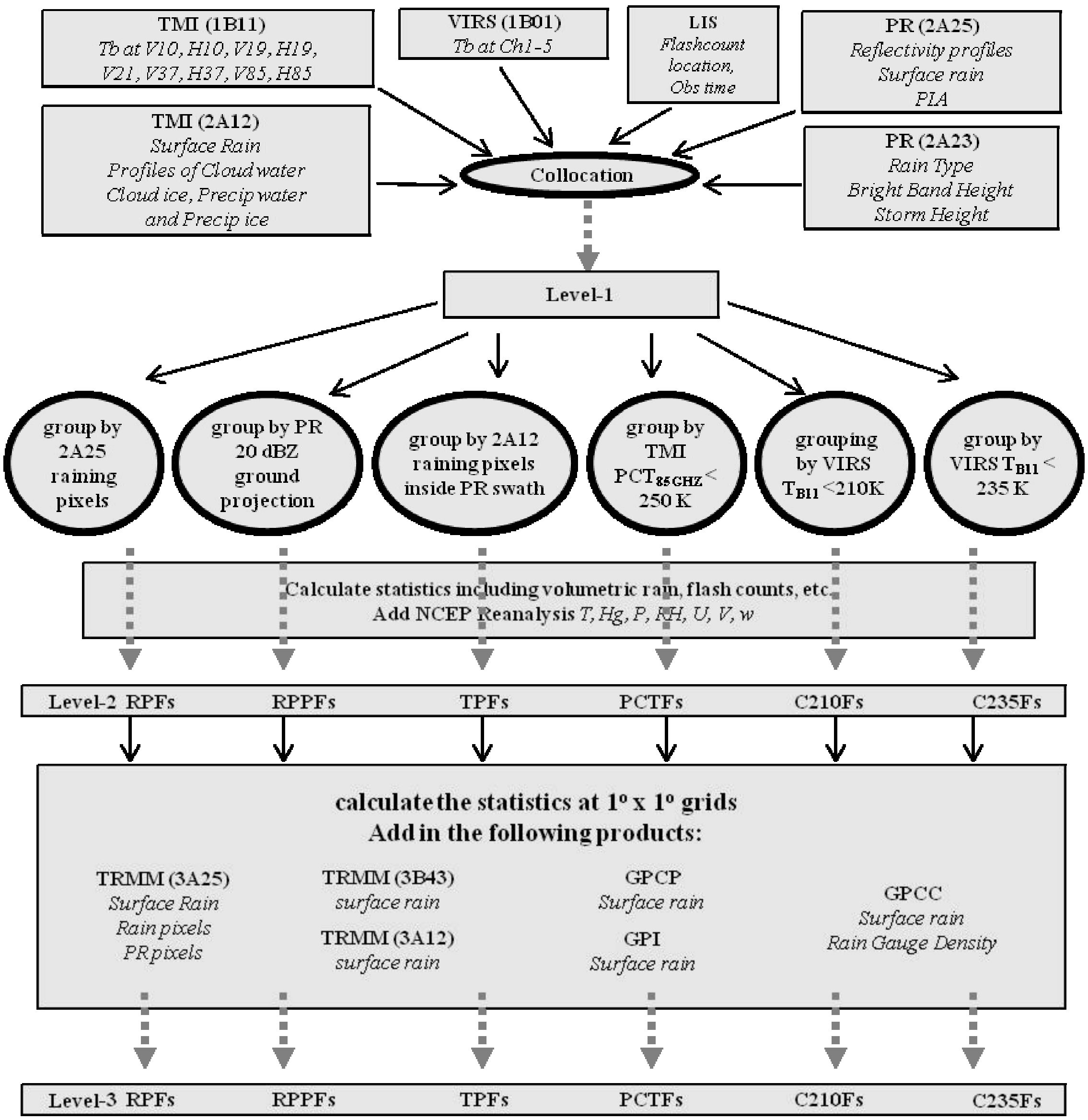

Figure 1. Flow chart of three levels of the University of Utah TRMM feature database. Here TMI T_b at V10, H10, V19, H19, V21, V37, H37, V85 and H85 stands for the vertical and horizontal polarized 10, 19, 21, 37 and 85 GHz brightness temperatures. VIRS Tb at Ch1-5 stands for the VIRS observed brightness temperatures at 0.65, 1.61, 3.75, 10.8, 12.0 µm wavelengths. This dataset is open to the public; anyone interested is encouraged to contact the authors for details.

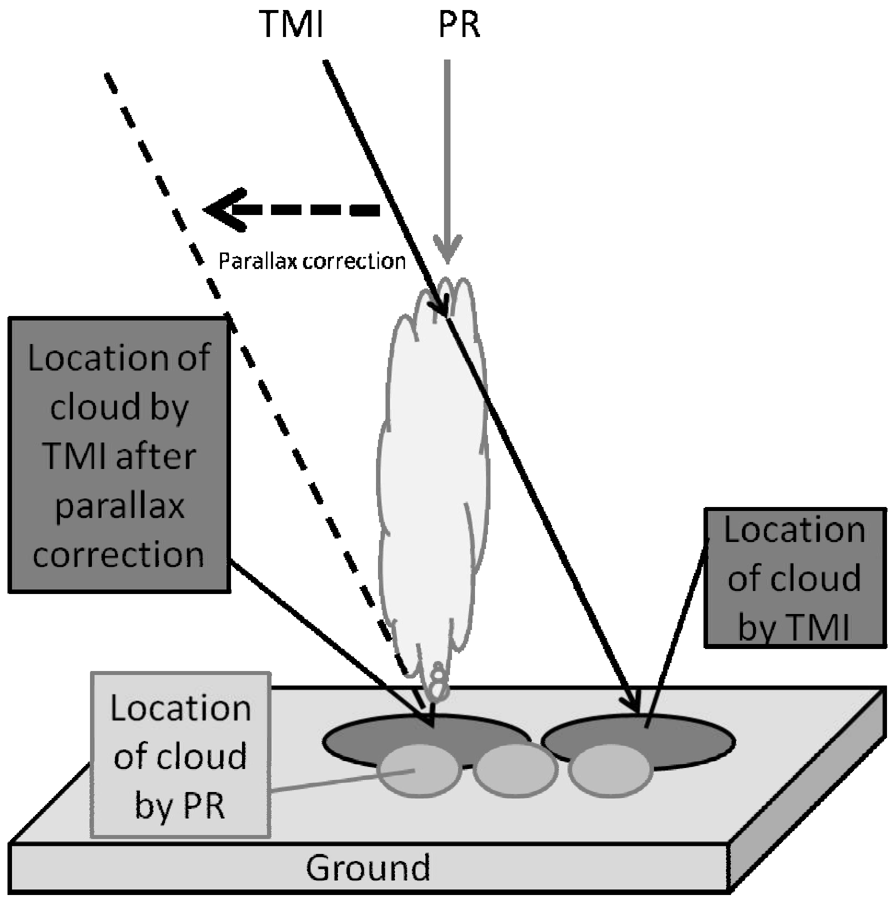

Figure 2. Schematic diagram of parallax correction. When there are hydrometeors at high altitude, the TMI microwave scattering signal would appear as from the nearby surface due to the 52^{o} slant angle. To account this effect and better collocate to the nadir observations, the TMI data coordinates are simply moved backwards (or forward depending on the orientation of the satellite) for one scan.

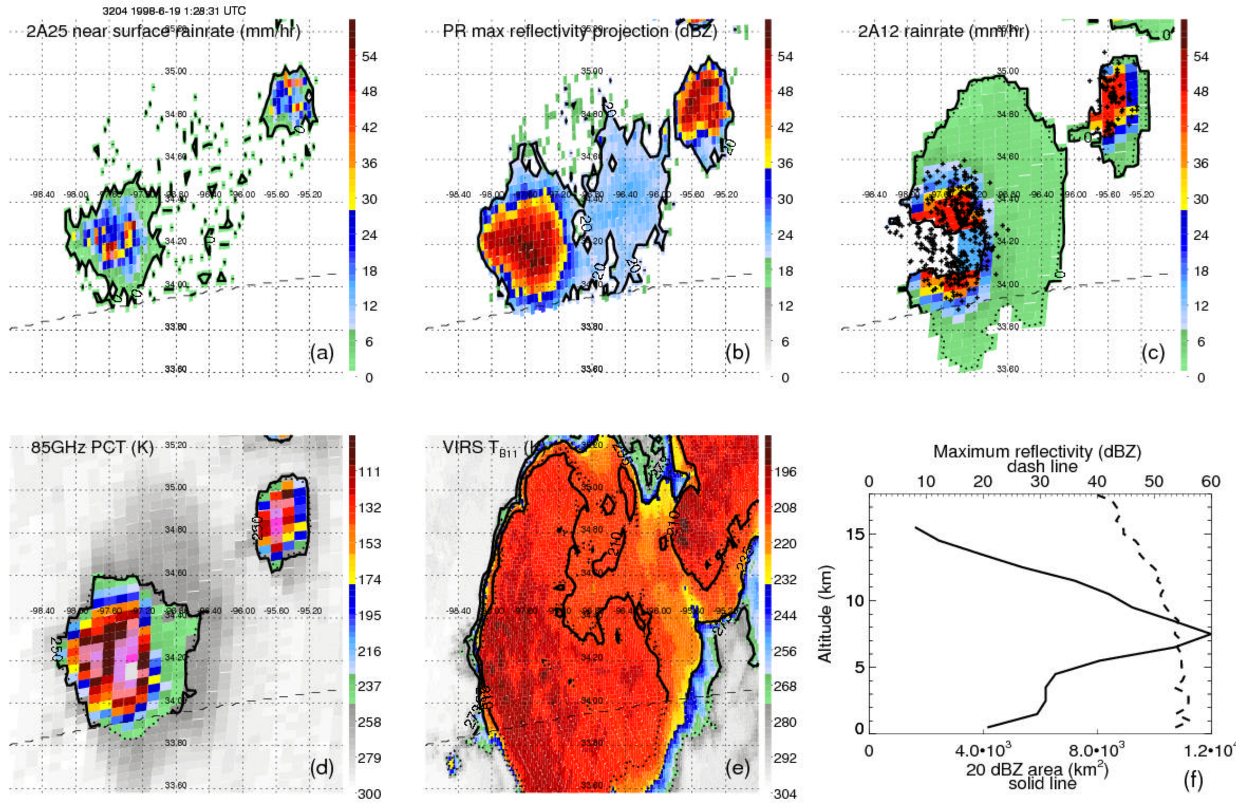

Figure 3. Demonstration of the feature types using a severe hail storm case (Zipser et al., 2006). a) 2A25 near surface rainfall rate. RPF is defined by the area with rain shown by black contour. b) PR maximum reflectivity ground projection. RPPF is defined by area with 20 dBZ shown by black contour. c) 2A12 surface rainfall rate. TPF is defined by area with rain shown by black contour. Black dots are the location of flashes detected by LIS. d) TMI 85 GHz PCT. PCTF is shown by 250 K contour line. e) VIRS T_{B11}. C210F, C235F and C273F are defined by area with T_{B11} < 210 K, 235 K and 273 K shown by black contours. f) Vertical profiles of 20 dBZ area and the maximum reflectivity of the large RPPF defined in b). The dash line in each panel is the edge of the PR swath. Note that there could be truncation effect due to narrow PR swath in defining large features (Nesbitt et al., 2006).

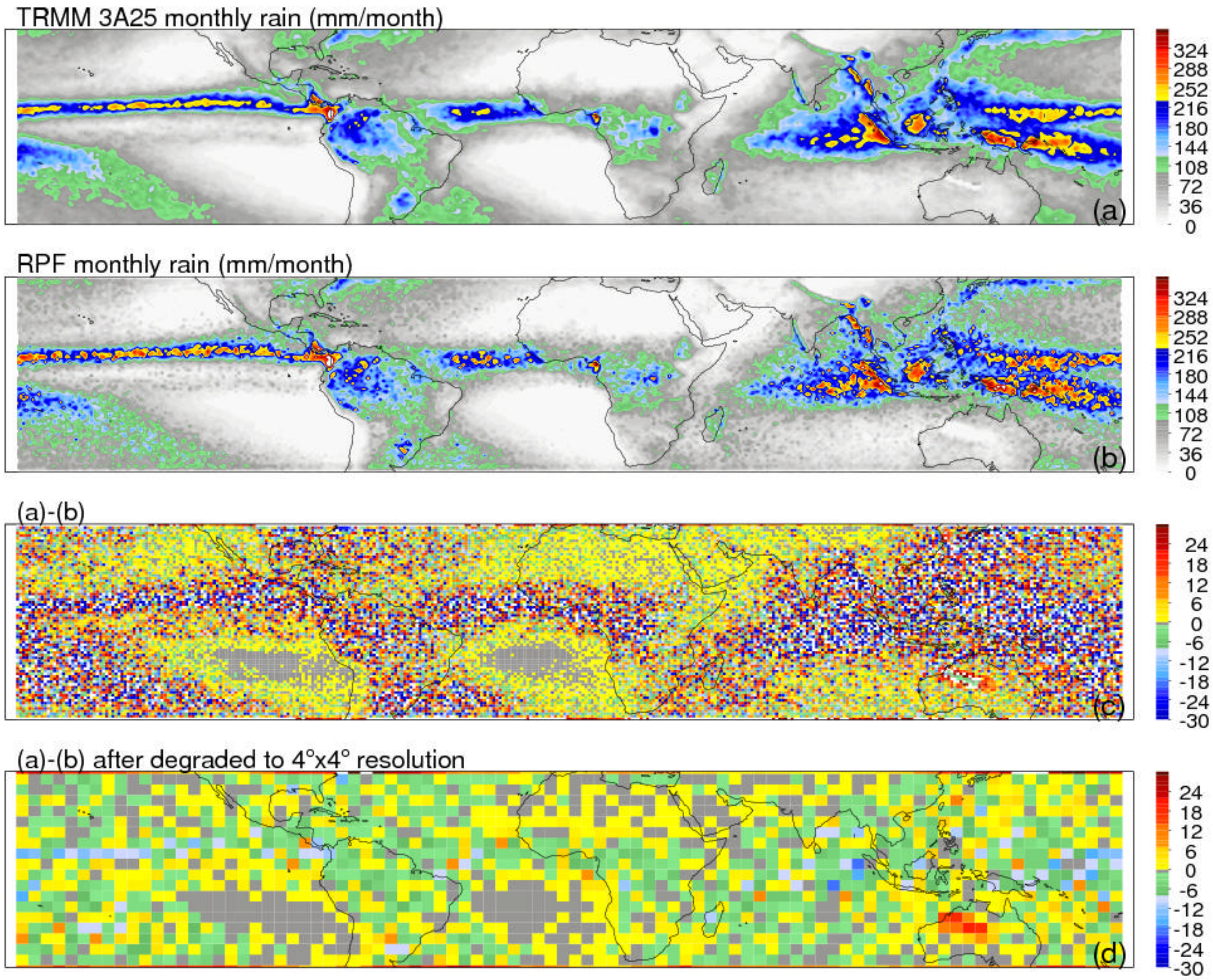

Figure 4. a) Mean TRMM 3A25 monthly rainfall from 1998-2006. b) Mean monthly rainfall from RPFs from 1998-2006. c) differences between (a) and (b). d) The differences between (a) and (b) after degrading them to 4^{o}x4^{o} resolution. Here negativevalues in c) and d) imply that more large precipitation systems are centered in the box so that the rainfall from nearby boxes has been counted in. Positive values in c) and d) imply that part of the rainfall in the box is from the large precipitation systems centered at nearby locations.

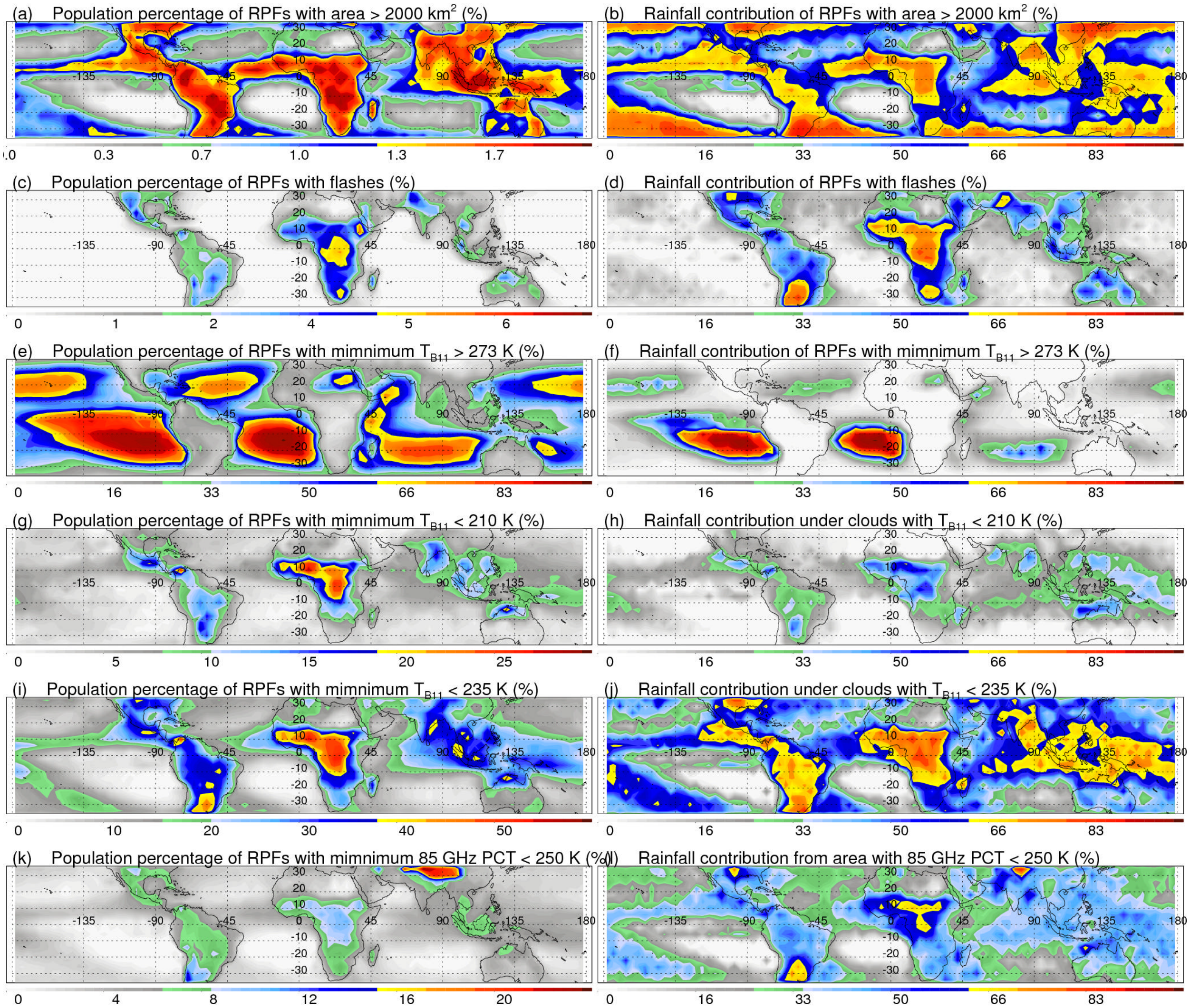

Figure 5. Distribution of population percentage of selected features to detectable features (at least with one PR pixel in size) and their regional rainfall contributions from 1998-2006 TRMM data. a) Population percentage of RPFs with size above 2000 km^2. b) Rainfall contribution from 2000 km^2 RPFs. c) Population percentage of RPFs with flashes. d) Rainfall contribution from RPFs with flashes. e) Population percentage of RPFs with minimum VIRS $T_{B11} > 273$ K. f) Rainfall contribution from RPFs minimum VIRS $T_{B11} > 273$ K. g) Population percentage of RPFs with minimum VIRS $T_{B11} < 210$ K. h) Rainfall contribution from area with VIRS $T_{B11} < 210$ K

(rainfall contribution from all C210Fs). i) Population percentage of RPFs with minimum VIRS $T_{B11} < 235$ K. j) Rainfall contribution from area with VIRS $T_{B11} < 235$ K (rainfall contribution from all C235Fs). k) Population percentage of RPFs with minimum TMI 85 GHz PCT < 250 K. l) Rainfall contribution from area with TMI 85 GHz PCT < 250 K (rainfall contribution from all PCTFs). Note that the scales change for the left panels (a,c,e,g,i,k).

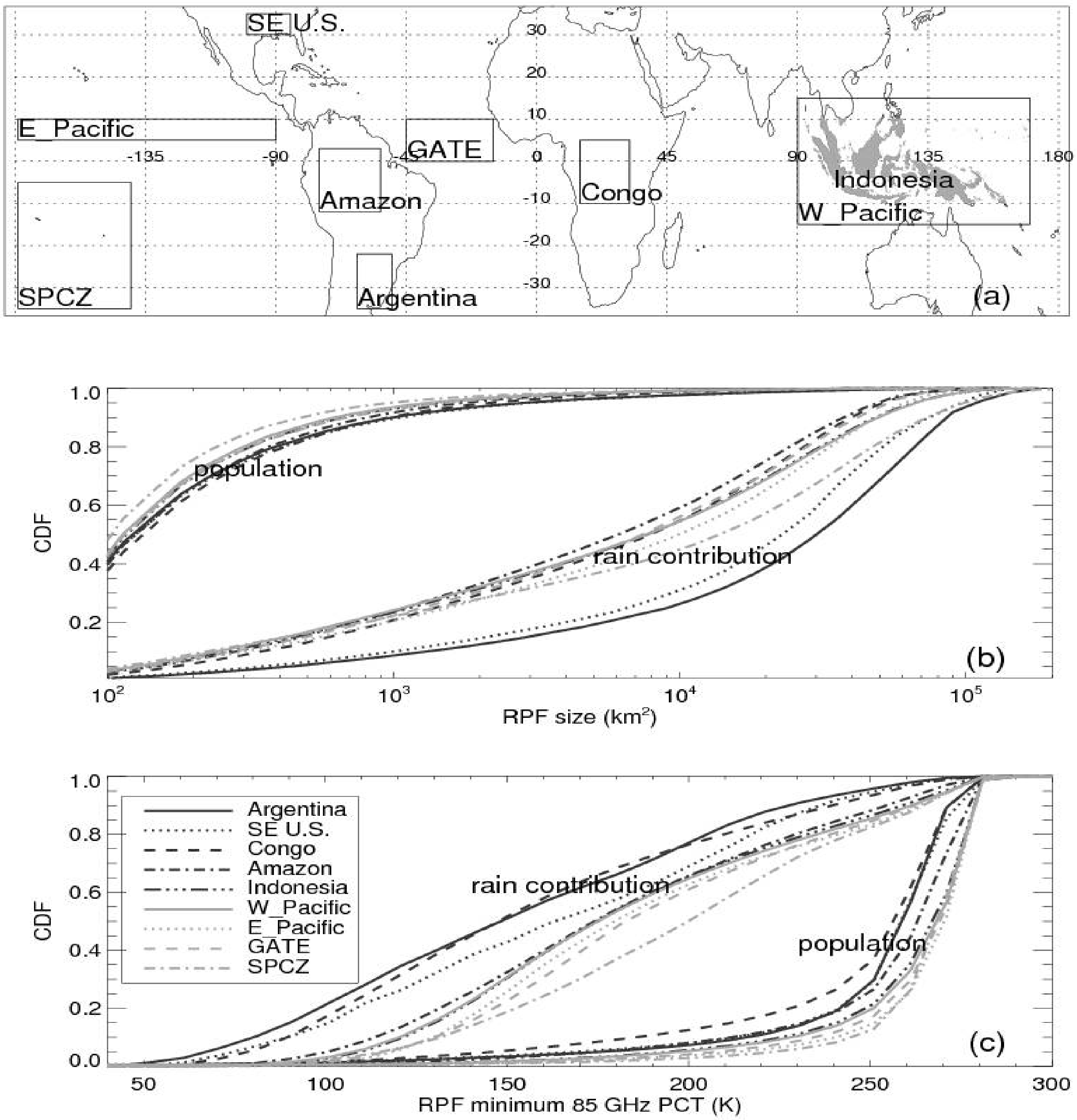

Figure 6. a) Map showing selected regions of interest. b) Cumulative distribution functions of sizes of the RPFs with at least 4 pixels and their rainfall contribution over the selected regions. c) Cumulative distribution functions of convective intensity of RPFs with at least 4 pixels inferred from 85 GHz PCT and their rainfall contribution over the selected regions.

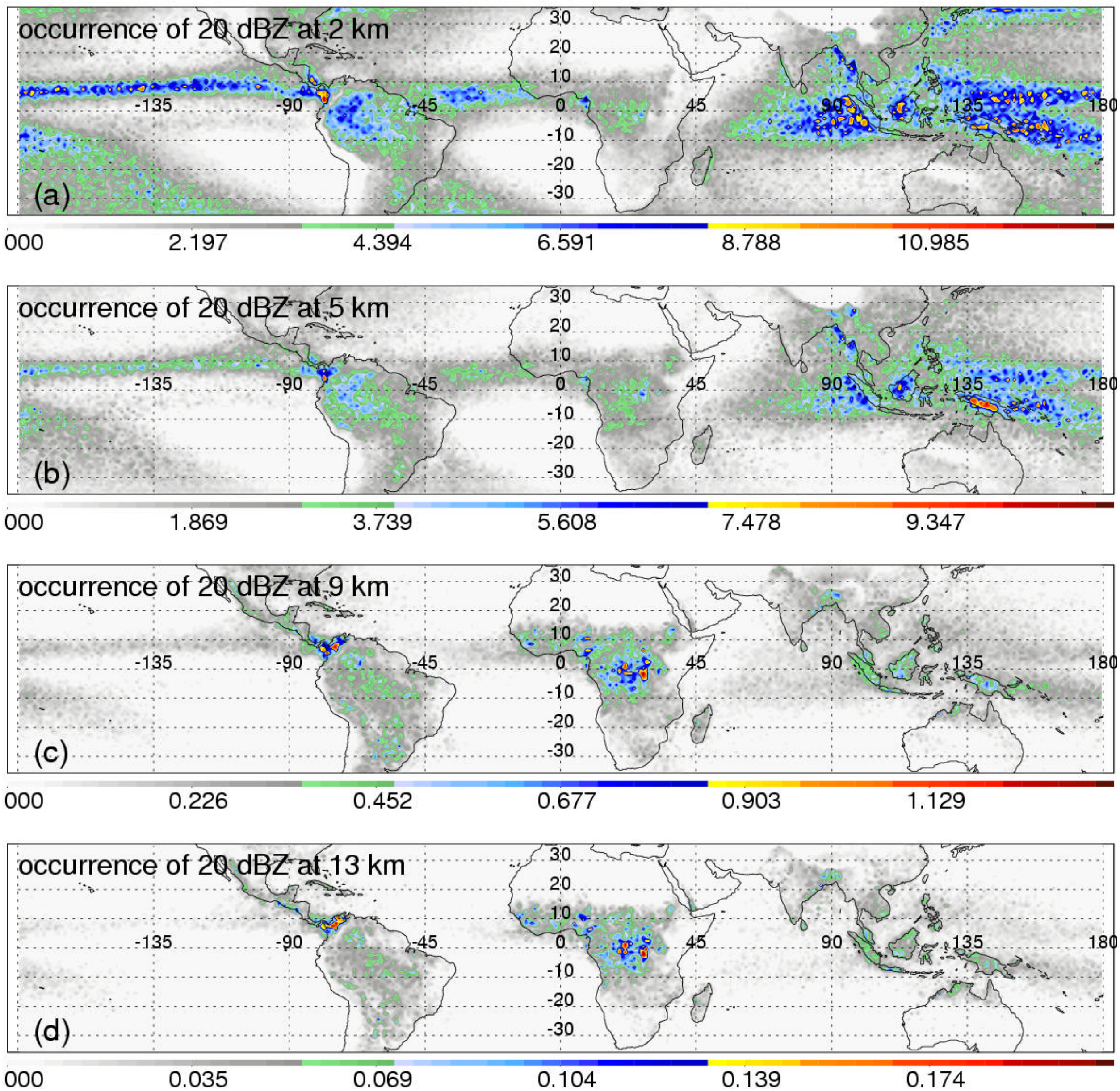

Figure 7. Occurrence of PR radar reflectivity above 20 dBZ at 1, 5, 9, and 13 km. The area of 20 dBZ are summarized from RPPFs in 1998-2006. Units are in %. Note that these heights are above the earth ellipsoid, so panel (a) cannot have echoes in regions of moderate terrain. Note that the scales are different for each panel.

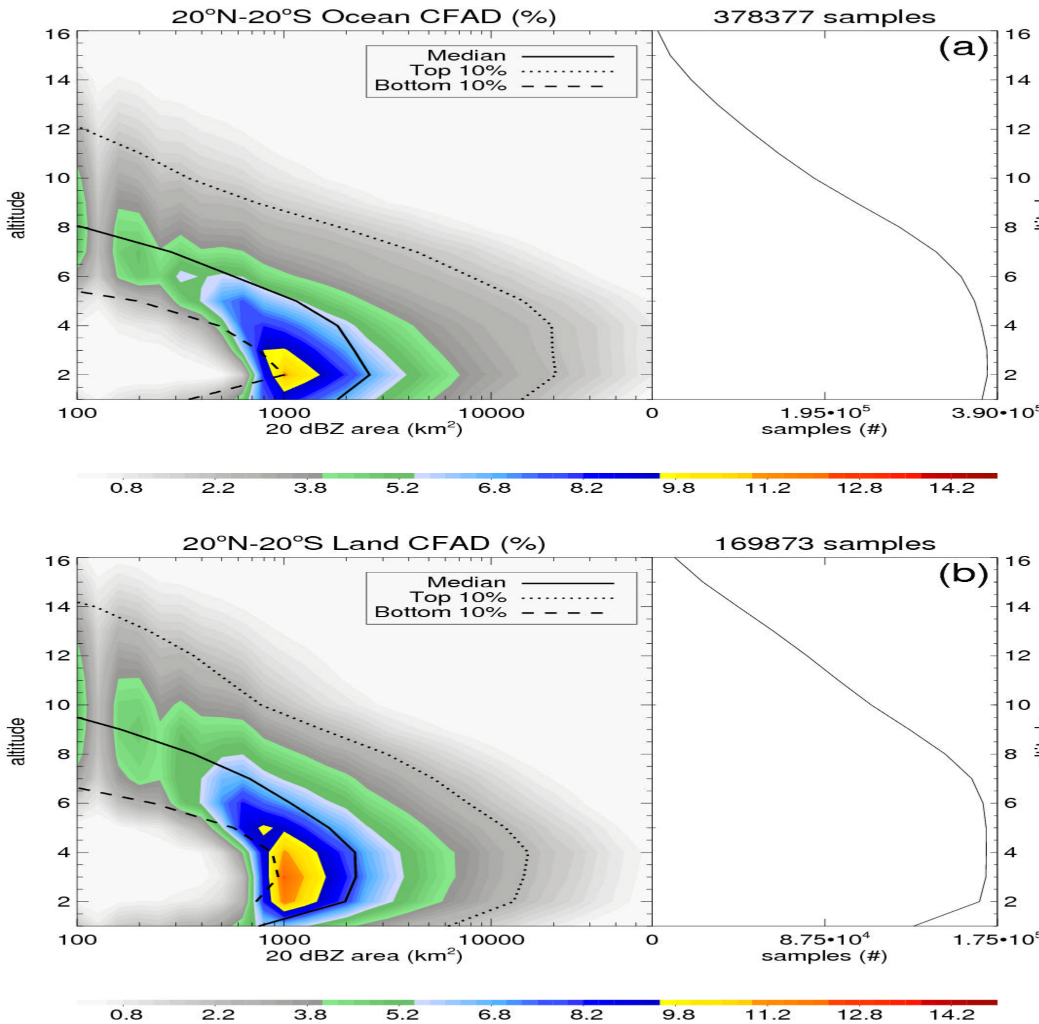

Figure 8. a) Frequency of 20 dBZ area at different altitudes from 1998-2005 20°N-20°S oceanic RPPFs with at least one 40 dBZ pixel and 1000 km^2 raining area. Median (solid line), top 10% (dot line) and bottom 10% (dash line) of 20 dBZ area values at different altitudes are shown. The frequency is calculated by determining the histogram of area of all RPPFs (including those with 0 km^2 area) at each altitude levels. Right panel shows the total number of non-zero RPPF samples with 20 dBZ at different altitudes. b) same as a), but for the RPPFs over land.

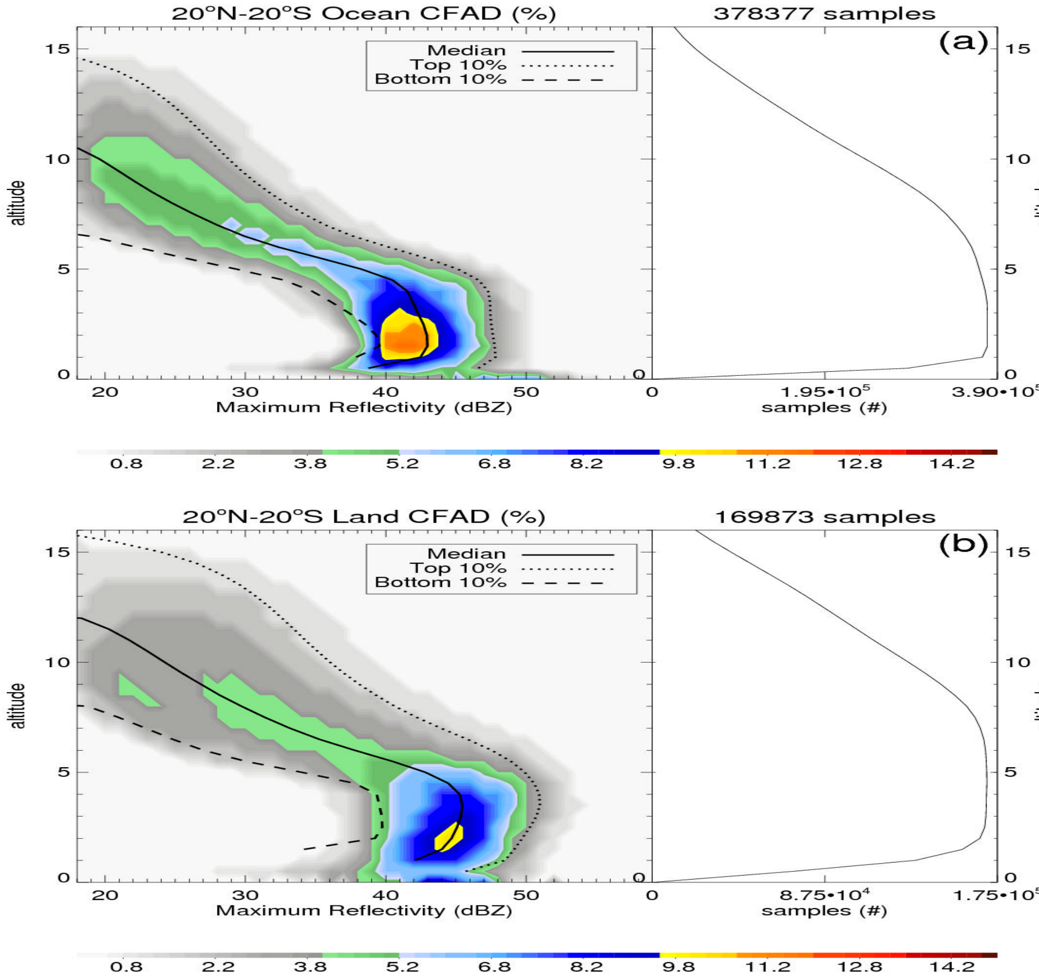

Figure 9. a) Frequency of maximum reflectivity at different altitudes from 1998-2005 20^{o}N-20^{o}S oceanic RPPFs with at least one 40 dBZ pixel and 1000 km^2 raining area. Median (solid line), top 10% (dot line) and bottom 10% (dash line) of maximum reflectivity values at different altitudes are shown. The frequency is calculated by determining the histogram of area of all RPPFs (including those without echoes) at each altitude levels. Right panel shows the total number of RPPF non-zero samples at different altitudes. b) same as a), but for the RPPFs over land. Note that the number of samples decreases sharply due to ground clutter contamination below 1.5 km over ocean and below 2 km over land.

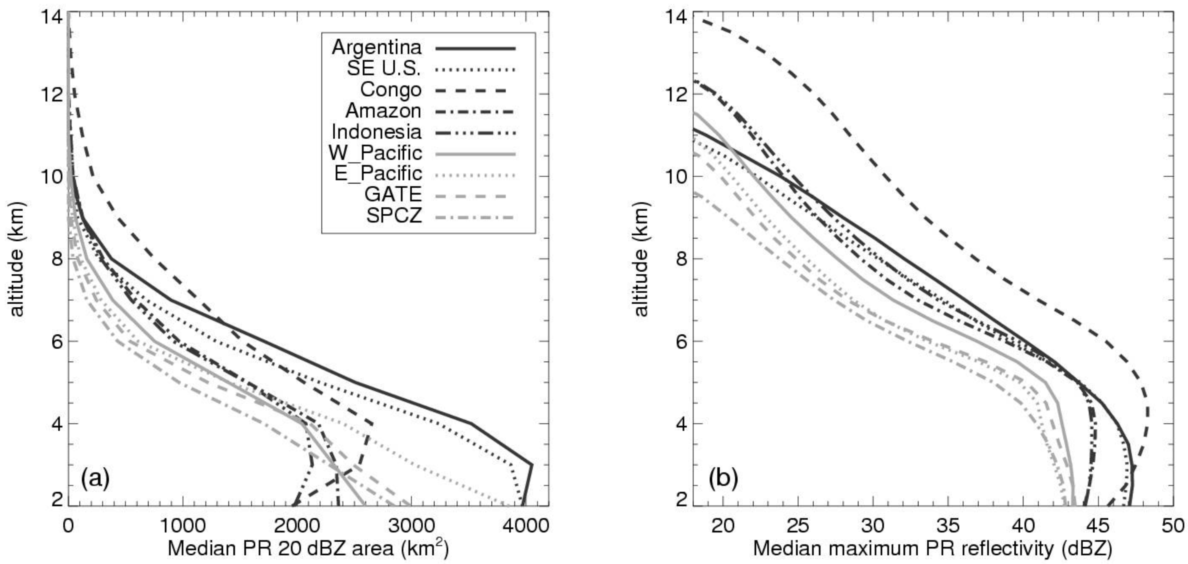

Figure 10. a) Median values of maximum reflectivity profiles from 1998-2006 RPPFs inside the selected regions shown in Figure 6a. The Median values are calculated in same way as the solid line shown in the left panel of Figure 8a) except from the RPPFs in the selected regions. b) same as a), but for the median values from 20 dBZ area profiles.